Spin Momentum–Locked Surface States in Metamaterials without Topological Transition

Liang Peng, Yuntian Chen,* Yihao Yang, Zhiyu Wang, Faxin Yu, Gaofeng Wang, Nian-Hai Shen, Baile Zhang, Costas M. Soukoulis, and Hongsheng Chen**

The photonic analogy of the quantum spin Hall Effect, that is, a photonic topological insulator (PTI), is of great relevance to science and technology in optics based on the promise of scattering-free surface states. The challenges in realizing such scattering-free surface states in PTIs and other types of symmetry-protected topological phases are the result of the exact symmetry needed for creating a pair of time reversal pseudo-spin states or special boundary conditions, wherein the exact symmetry imposes strict requirements on materials or boundary conditions. Here, it is experimentally demonstrated that scattering-free edge states can be created with neither the aforementioned exact symmetry requirements for materials nor the topological transitions. This system is constructed by simply placing together regular homogeneous metamaterials, which are characterized by highly different bianisotropies. Of the particular surface states, backward reflection would be deeply suppressed, provided that the related evanescent tail into the bulk regions vanishes shortly and that the pseudo-spin is not flipped by the scatterers. This work gives an example of constructing scattering-free surface states in classical systems without strict symmetry protections and may potentially stimulate various novel applications in the future.

1. Introduction

If photonic topological insulators (PTIs) with different topological invariants are placed together, gapless edge states are excited, leading to robustness against defects.[1–11] The key to realizing PTIs is to construct a time reversal pair of pseudo-spin states that resemble the electron spin as well as to introduce the spin–orbit interaction of light,[9,12] which are very challenging tasks. Indeed, the material realization in PTIs for constructing pseudo-spin states with exact time reversal symmetry in combination with strong spin–orbit interaction is rather difficult, commonly requiring the ε/μ match. It is well understood that the spin–orbit interaction of light generates an opposite artificial magnetic field for the two decoupled spin sectors, that is, two copies of quantum hall states, where the topological transition occurs. By the bulk surface principle, the surface state is ensured, leading to gapless edge states that are robust against non-magnetic scatters. The above interesting features of the PTIs are essentially protected by the time reversal symmetry. This type of global symmetry, that is, time reversal symmetry, can be extended to other types of symmetry-protected topological orders by special boundary conditions.[13–18]

The argument of symmetry exactness has been routinely used in the construction of topologically trivial and non-trivial back-scattering free edge states in homogeneous materials.[19]

Prof. L. Peng, Prof. G. Wang
Key Laboratory for RF Circuits and Systems
Hangzhou Dianzi University
Ministry of Education
Hangzhou 310018, China
E-mail: pengl@hdu.edu.cn

Dr. Y. Chen
School of Optical and Electronic Information
Huazhong University of Science and Technology
Wuhan 430074, China
E-mail: yuntian@hust.edu.cn

Dr. Y. Yang, Prof. H. Chen
State Key Laboratory of Modern Optical Instrumentation
Zhejiang University
Hangzhou 310027, China
E-mail: hansomchen@zju.edu.cn

Prof. Z. Wang, Prof. F. Yu
School of Aeronautics and Astronautics
Zhejiang University
Hangzhou 310027, China

Dr. N.-H. Shen, Prof. C. M. Soukoulis
Department of Physics and Astronomy and Ames Laboratory-U.S. DOE
Iowa State University
Ames IA 50011, USA

Prof. B. Zhang
Division of Physics and Applied Physics
School of Physical and Mathematical Sciences
Nanyang Technological University
Singapore 637371, Singapore

Prof. C. M. Soukoulis
Institute of Electronic Structure and Laser
FORTH 71110, Heraklion, Crete, Greece

DOI: 10.1002/lpor.201800002

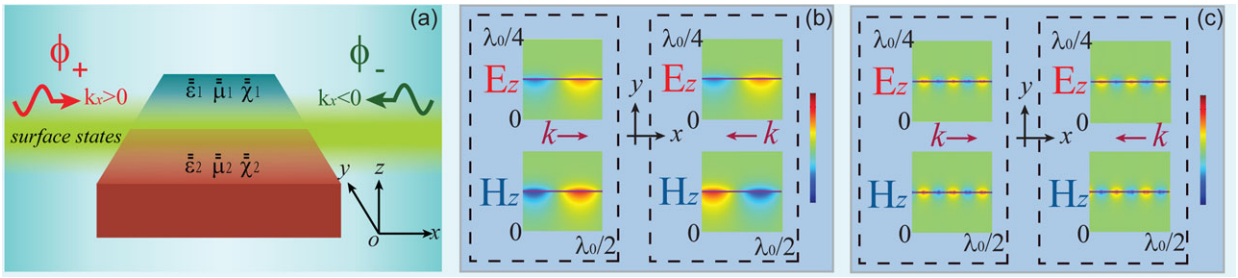

Figure 1. a) Two homogeneous bulks are placed together to form an interface supporting HSS. b) The E_z and H_z distribution of the HSS with $\chi_1 = 1.5$ and $\chi_2 = -5$. c) The E_z and H_z distributions of HSS with $\chi_1 = 1.5$ and $\chi_2 = 5$. In all the calculations and simulations, $\bar{\bar{\varepsilon}} = \text{diag}[2, 2, 4]$ and $\mu_1 = \mu_2 = 1$. It is obvious that for $\text{sgn}(\chi_1) = \pm\text{sgn}(\chi_2)$, a certain HSS could be excited at the interface.

However, the exact symmetry, that is, either PTIs by time reversal symmetry or other symmetry-protected topological phases, could potentially give rise to experimental complications in the material realizations. Thus, it is a natural question to ask whether the exact symmetry is the necessary condition to realize scattering-free edge states or if such a requirement of exact symmetry can be lifted.

In this work, we attempt to answer the question by demonstrating the excitation of surface states with a spin momentum–locking (SML) feature using homogeneous bulk metamaterials. We show that by setting the bianisotropy of two adjacent bulks as being dramatically different, with either similar or reversed signs, surface states of a certain type are successfully excited by hybridizing the fundamental modes. Further study reveals the spin momentum–locked pseudo-spin profile of the surface states, due to which backward scattering decreases. In addition, a method of achieving nearly zero reflection is presented. By combining two perpendicular split-ring resonators, two homogeneous bulks with highly different bianisotropies are designed and fabricated. With this enhanced bianisotropy, an overlapped forbidden band is opened to both of the bulk metamaterials. In experiments, the hybrid surface states are successfully excited at the interface between the two forbidden bulks; in addition, a nearly zero backscattering effect is observed.

2. Hybrid Surface Waves by Bianisotropy

It is a common case that surface waves are generally excited on interfaces where material transition occurs, to which negative constitutives are usually applied.[20] However, here we alternatively use the bianisotropy transition instead, so that the magneto-electric (ME) effect can be intrinsically obtained in realizing pseudo-spin polarization, as we show below. The constitutive relations for the homogeneous metamaterials take the form $\bar{D} = \varepsilon_0\bar{\bar{\varepsilon}} \cdot \bar{E} + i\sqrt{\varepsilon_0\mu_0}\bar{\bar{\chi}} \cdot \bar{H}$ and $\bar{B} = \mu_0\bar{\bar{\mu}} \cdot \bar{H} - i\sqrt{\varepsilon_0\mu_0}\bar{\bar{\chi}}^T \cdot \bar{E}$, where $\bar{\bar{\varepsilon}}$ and $\bar{\bar{\mu}}$ are permittivity and permeability tensors and $\bar{\bar{\chi}}$ is the magneto-electric tensor. For simplicity, we consider that the material is reciprocal and has rotational symmetry about the z-axis with an isotropic dispersion in the x-y plane, that is, $\bar{\bar{\varepsilon}} = \text{diag}[\varepsilon_t, \varepsilon_t, \varepsilon_z]$ and $\bar{\bar{\mu}} = \text{diag}[\mu_t, \mu_t, \mu_z]$. For $\bar{\bar{\chi}}$, we assume $\chi_{xy} = -\chi_{yx} = \chi$, while all the other elements are zero. Under this assumption, the chirality of the material is zero so that the fundamental modes are separated through their polarizations (similar to TE and TM decoupling),[21] which makes the topological invariants vanish for regular non-dispersive materials.[22] Moreover, this assumption reduces the difficulty of material design and fabrication since the magneto-electric (ME) effect of a planar structure can only make the perpendicular $\bar{E}$ and $\bar{H}$ be coupled such as in unbalanced split-ring resonators(USRRs).[9,23–25]

Now, we focus on the in-plane (x-y) propagation of electromagnetic (EM) modes inside the metamaterial, which can be conveniently solved with the source-free Maxwell's equations.[26] It is straightforward to show that the characteristic polarization in the uniform metamaterial can be clarified as two decoupled types, that is, the transverse electric (TE) like type ($E_z = 0$) and the transverse magnetic (TM) like type ($H_z = 0$). However, if there exists a boundary, or a scatterer, these two types cannot propagate independently. In particular, a non-zero $\bar{\bar{\chi}}$, the localized states would be mixed. Specifically, hybridizing the TE-like and TM-like types is essential to ensure boundary continuity, as we will show further.

Without loss of generality, two metamaterial bulks with ($\bar{\bar{\varepsilon}}_1$, $\bar{\bar{\mu}}_1$, $\bar{\bar{\chi}}_1$) and ($\bar{\bar{\varepsilon}}_2$, $\bar{\bar{\mu}}_2$, $\bar{\bar{\chi}}_2$) are placed together, as shown in **Figure 1**a. Let the boundary be parallel to the x-axis; then, in ensuring field continuity,[26,27] we require that $\hat{y} \times \bar{E}|_{y=0^-} = \hat{y} \times \bar{E}|_{y=0^+}$ and $\hat{y} \times \bar{H}|_{y=0^-} = \hat{y} \times \bar{H}|_{y=0^+}$. Together with Maxwell's equations, the relationship between different field components can be determined (see Supporting Information). With both E_z and H_z being non-zero, we derive

$$(\mu_{t,1}k_{y,\text{TE},1} - \mu_{t,2}\gamma k_{y,\text{TE},2})(\varepsilon_{t,1}k_{y,\text{TM},1} - \varepsilon_{t,2}\gamma k_{y,\text{TM},2}) = -(\chi_1 - \chi_2\gamma)^2 k_x^2 \quad (1)$$

where $\gamma = \beta_1/\beta_2$, $\beta_j = \varepsilon_{t,j}\mu_{t,j} - \chi_j^2$, $k_{y,\text{TE},j} = \sqrt{k_0^2\beta_j\mu_{z,j}/\mu_{t,j} - k_x^2}$, and $k_{y,\text{TM},j} = \sqrt{k_0^2\beta_j\varepsilon_{z,j}/\varepsilon_{t,j} - k_x^2}$ ($j = 1, 2$). Equation (1) exhibits the dispersion for the hybrid surface states (HSS). Due to its complexity, the closed-form solution cannot readily be obtained. Numerical evaluations would facilitate comprehensive studies of the HSS. We emphasize that in exciting the HSS, it is essential to have real k_x and imaginary k_y, that is, $k_{y,1} = i|k_{y,1}|$ and $k_{y,2} = -i|k_{y,2}|$, so that all the fields decay exponentially in the $\pm\hat{y}$ directions.

To show the existence of the HSS, here, we assume that all the elements in $\bar{\bar{\varepsilon}}_1$, $\bar{\bar{\mu}}_1$, $\bar{\bar{\varepsilon}}_2$, and $\bar{\bar{\mu}}_2$ are positive, with $\varepsilon_{t,1}\mu_{t,1} < \chi_1^2$ and $\varepsilon_{t,2}\mu_{t,2} < \chi_2^2$. With this, both of the bulks are fully cut off so that imaginary k_y would be ensured with any real-valued k_x, which

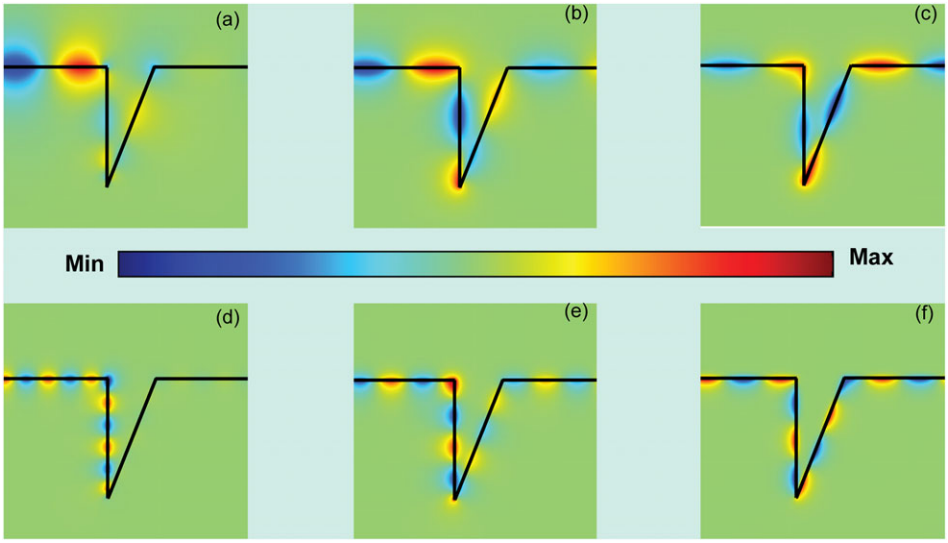

Figure 2. The H_z distribution in various HSSs encountering a fabricating defect. In the simulations, the excitation source is z polarized, and $\varepsilon_{t,1} = \varepsilon_{t,2} = 2$, $\varepsilon_{z,1} = \varepsilon_{z,2} = 4$, and $\mu_1 = \mu_2 = 1$. For the bianisotropy, we set a) $\chi_1 = -\chi_2 = 1.5$; b) $\chi_1 = -\chi_2 = 3$; c) $\chi_1 = -\chi_2 = 5$; d) $\chi_1 = 1.5$, $\chi_2 = 5$; e) $\chi_1 = 2.25$, $\chi_2 = 7.5$; and f) $\chi_1 = 6$, $\chi_2 = 20$. It is obvious that the backscattering is gradually suppressed when enhancing the bianisotropy. In all the simulations, HSS comes from the left side.

simplifies the validation and prevents the power leakage of the HSSs. Numerical evaluation shows that a solution of Equation (1) can always be obtained for almost all values of bianisotropy. For additional details, please refer to Supporting Information.

In Figures 1b,c, we show the field distribution for $\mathrm{sgn}(\chi_1) = \mp\mathrm{sgn}(\chi_2)$, respectively. The field profiles are similar for both cases. Again, from these figures, we find that E_z and H_z of the specified HSSs would be either in phase or out of phase, which is k_x-dependent. The relationship between the hybrid polarization and k_x can be described by the following master equation:

$$\varphi_{\pm} = \pm\frac{\chi_1 - \chi_2\gamma}{AB}k_x\varphi_{\pm} \tag{2}$$

with $\varphi_{\pm} = AE_z|_{y=0} \pm B\eta_0 H_z|_{y=0}$, $A = \sqrt{\varepsilon_{t,1}|k_{y,\mathrm{TM},1}| + \varepsilon_{t,2}\gamma|k_{y,\mathrm{TM},2}|}$ and $B = \sqrt{\mu_{t,1}|k_{y,\mathrm{TE},1}| + \mu_{t,2}\gamma|k_{y,\mathrm{TE},2}|}$. Noting that k_x can be safely replaced by $-i\partial_x$, we can regard the HSS as a type of pseudo-spin states. However, the specified pseudo-spin states do not spread into the entire bulks; rather, they are bounded at the interface, unlike that of the PTIs. It is evident that the distinguished hybridization of E_z and H_z is protected by the time reversal symmetry and emulates the SML in photonics.[9,28] The straightforward outcome is that sources polarized with the in-phased E_z and H_z with a specified magnitude can only excite the $k_x > 0$ waves. Moreover, objects with an identical polarization property are not able to flip the pseudo-spins, so backscattering can be avoided, according to a mode-matching analysis (see Supporting Information). However, the requirement for backscattering immunity is hardly ensured in common cases because the scatterers may be arbitrary. Alternatively, it is meaningful to discuss the backscattering suppression in the case where the supporting interface is perturbed.

Without loss of generality, we assume that $\bar{\bar{\varepsilon}}_1 = \bar{\bar{\varepsilon}}_2$ and $\bar{\bar{\mu}}_1 = \bar{\bar{\mu}}_2$. To test the reduction in backward scattering, we assume that there is a fabricating defect at the interface, as shown in **Figure 2**a. It is seen that three corners are involved in the defect, corresponding to angles of 90°, 21.8°, and 111.8°. For the simulations in Figures 2a–c, the bulks exhibit bianisotropies of $\chi_1 = -\chi_2 = 1.5$, $\chi_1 = -\chi_2 = 3$, and $\chi_1 = -\chi_2 = 5$. In Figure 2a, we see that the HSS is excited at the boundary but fails to continue through the 90° corner. In Figure 2b, the bianisotropy is enhanced; as a result, the HSS can successfully overcome the 90° corner but is still blocked by the 21.8° corner. The 21.8° corner is overcome by further enhancing the bianisotropy, and consequently, the reflection from each corner becomes negligible, as shown in Figure 2c. For Figures 2a–c, the increment of the bianisotropy leads to a faster decay of evanescent tails into the bulks; as a result, the reflections from the sharp corners are strongly suppressed. The interpretation for this effect is regarded as a phase disturbance by the sharp corners, that is, because of the non-vanishing evanescent waves, the passage of power flow can be equivalently treated as a conduit; once there exists a sharp corner, the EM power in different parts of the conduit may suffer from different phase shifting, and hence, scattering occurs. By enhancing the bianisotropy, the evanescent tail of the HSS shrinks, and thus, the power conduit becomes thinner, which reduces the relative phase shifting.

In the case $\mathrm{sgn}(\chi_1) = \mathrm{sgn}(\chi_2)$, the excitation of the HSS is also observed when the contrast of the bianisotropy is sufficiently large. In Figures 2d–f, we show that the HSSs are excited when $\chi_2 > 3\chi_1$. In Figure 2d, the HSS exhibits sensitivity to the corners. By gradually enhancing the bianisotropy, the evanescent tail is further reduced; then, suppressed backscattering is again realized, as shown in Figures 2e, f.

3. Metamaterial Design and Fabrication

In our work, we design two metamaterials. The bianisotropy of one metamaterial is much higher than that of the other. In the

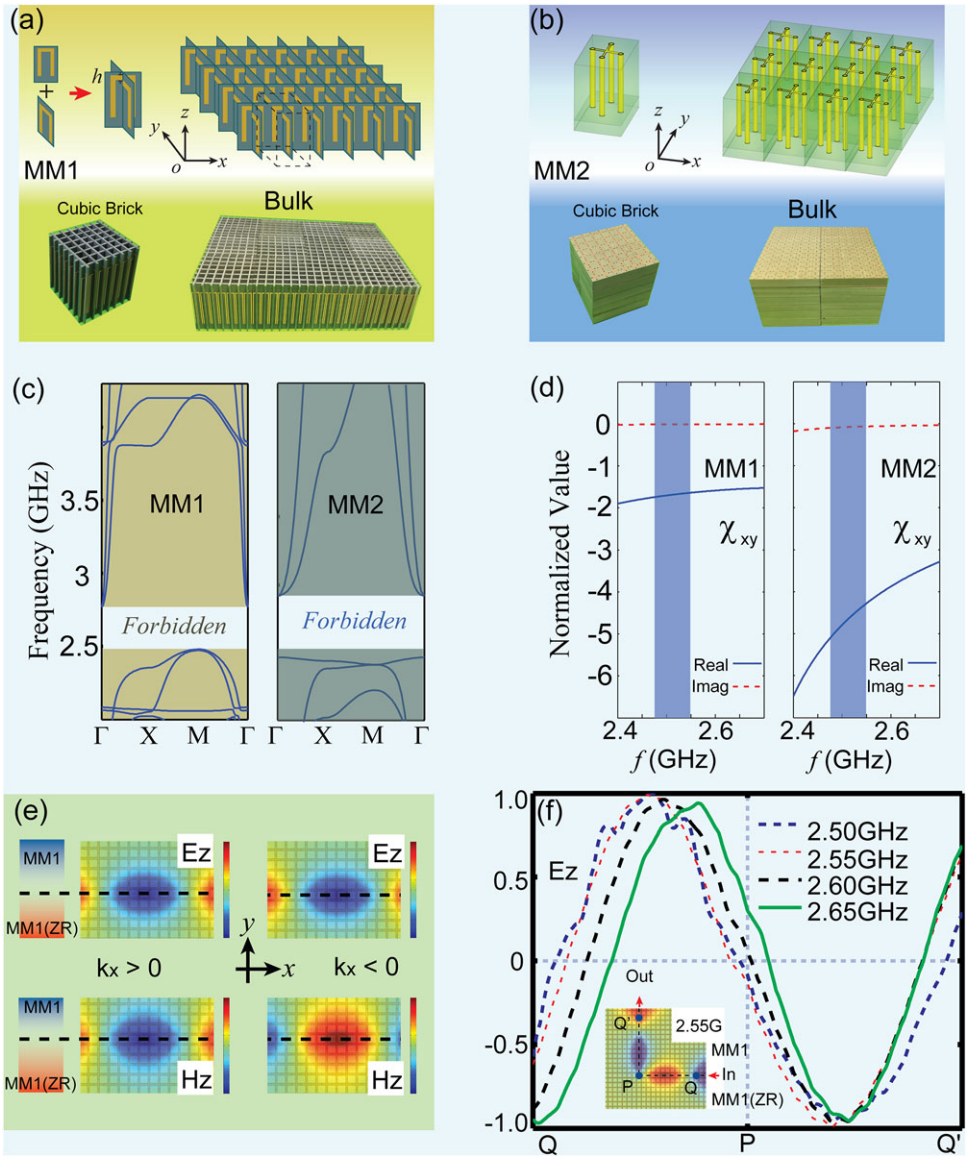

Figure 3. The design of two metamaterials and full-wave simulations. a) MM1: designed by crossing two perpendicular USRRs. Upper: schematics; Lower: fabricated bulk. The USRR is fabricated on the PTFE/glass polymer (F4B) substrate (a PCB board with $\varepsilon_r = 2.65$ and $\sigma = 0.003$), and $7 \times 7 \times 1$ unit cells are fused together to form a cubic brick. b) MM2: designed by opening through holes on a TP substrate, where four holes are connected on one side of the substrate to form a unit cell. Upper: schematics; Lower: fabricated bulk. $7 \times 7 \times 5$ unit cells are used to construct a cubic brick. c) Band structures for MM1 and MM2. The two forbidden bands are designed to overlap from below 2.5 GHz to above 2.7 GHz. In the band diagram, the two modes at the same frequency stand for the TE and TM polarizations, respectively. d) The extracted bianisotropy for the two metamaterials. Using a substrate with a high dielectric constant, MM2 can have a bianisotropy that is much higher than that of MM1. The shadow region represents the band for a possible HSS with $\mathrm{sgn}(\chi_1) = \mathrm{sgn}(\chi_2)$, as estimated using the retrieved parameters. e) The full-wave simulations of E_z and H_z in the HSS. The interface is formed by MM1 with the lower half part of the material being z-reversed. The φ_+ and φ_- states for $k_x > 0$ and $k_x < 0$ waves reveal the spin momentum–locking of the HSS. f) The simulated E_z distribution shows backscattering suppression by the HSS.

design, the off-diagonal elements in $\bar{\bar{\chi}}$ are realized by the USRR. By combining two perpendicular USRRs with rotational symmetry, the specified bianisotropy can be achieved.

The first metamaterial (MM1) is realized by crossing two identical printed circuit board (PCB) based USRR arrays. The structure and schematics of MM1 are shown in **Figure 3**a. To reduce the difficulty of fabrication, the USRRs are combined at a distance h in the z-direction so that overlapping of the metals is avoided. During fabrication, $7 \times 7 \times 1$ unit cells are fused together to form a cubic MM1 brick with dimensions of $35 \times 35 \times 35$ mm. In Figure 3b, the second metamaterial (MM2) is fabricated by adding conducting holes on a low loss ceramic substrate (TP substrate, with $\varepsilon_r = 16$ and $\sigma = 0.003$) and then connecting four holes to form a single unit cell on one of the substrate's

side. During fabrication, $7 \times 7 \times 5$ unit cells are fused together to form a cubic brick with an overall size identical to the previous metamaterial. For detailed information about MM1 and MM2, please refer to Supporting Information. We emphasize here that the bianisotropy of these two metamaterials is drastically different because of the contrast in the constructing substrate. The mechanism for the bianisotropy manipulation is not discussed in the present context; numerical evaluations would demonstrate the validity of our work.

For the two metamaterials, the effective parameters are intrinsically dispersive due to the ME resonance,[9,29,30] that is, ε_t and μ_t might be smaller than χ, which stops both the TE and TM modes (see Supporting Information), and hence, a forbidden band could be expected beyond the resonant frequency. The metamaterials' effective parameters may be extracted through the retrieval approach.[31] However, the effective parameters are not able to precisely estimate the forbidden band in the spatially dispersive case because of the unavoidable Bloch scattering in periodic structures.[32] As a result, eigenmode simulations for a single unit cell are conducted to predict the exact forbidden band. By carefully tuning the dimensions of the USRRs, the forbidden bands of MM1 and MM2 overlap. The full band structures of the two metamaterials are shown in Figure 3c. We see that both of the forbidden bands expand from below 2.5 GHz to above 2.7 GHz. At the upper bound of the forbidden band, two fundamental modes, that is, the TE-like and TM-like modes, degenerate and cease propagating simultaneously, indicating the possible transition of $\varepsilon_t\mu_t > \chi^2$ to $\varepsilon_t\mu_t < \chi^2$, because the homogenization of the metamaterials holds at the Γ point.[32,33] At other points (X and M) in the Brillouin zone (BZ), although affected by the Bloch scattering, the band structures remain forbidden to both TE-like and TM-like waves. On the other hand, through the parameter retrieval approach, the effective magneto-electric coefficients (χ_{xy}) for both of the metamaterials are extracted, as shown in Figure 3d. It is seen that χ_{xy} for both metamaterials is enhanced inside the forbidden band. However, MM1 and MM2 have a large contrast in χ_{xy}, as previously stated. As a result, it is expected that the HSS can be excited by combining the two metamaterial bulks. In particular, if the bianisotropies of the two bulks have the same sign, that is, $\mathrm{sgn}(\chi_1) = \mathrm{sgn}(\chi_2)$, the HSS is expected to be in a narrow range at approximately 2.5 GHz, as indicated by the shadow region in Figure 3d.

Full-wave simulations for large-area bulks are also conducted. In Figure 3e, E_z and H_z of the HSS are shown. In the figure, a passage is formed by MM1, with the lower half of the material being z-reversed (ZR). It is seen that two HSSs are formed by linearly combining the TE and TM polarizations, that is, the phase difference between E_z and H_z is distinguished by a factor of π for $k_x > 0$ and $k_x < 0$, as theoretically predicted. To test the backscattering reduction, a bent passage is designed; see the Q-P-Q' in the inset of Figure 3f. Because of the C_4 symmetry of MM1, a 90° sharp corner is allowed at the P point. The HSS enters the passage at Q, changes its direction at P, and then leaves the path at Q'. We note that the sharp corner with infinite curvature cannot be finely emulated by metamaterials because of the finite sized cells such that the influence of the evanescent tail would be reduced. Then, it is expected that the HSS will be able to pass through the 90° bend with negligible reflection; see the extracted E_z distributions for four different frequencies in Figure 3f. In the inset, the 2D E_z field distribution at 2.55 GHz is shown. It is seen that the amplitude of E_z remains unchanged and that the phase is continuous across the bending at P. We note that the nearly zero-reflection property holds across the forbidden band, which is hardly achieved through conventional waveguides.

The simulated field distributions for the other HSS can be found in Supporting Information. We observe that the HSS supported by $\mathrm{sgn}(\chi_1) = -\mathrm{sgn}(\chi_2)$ possesses a wavelength that is much longer than the periodicity and hence is steady and well behaved. However, for the HSS supported by $\mathrm{sgn}(\chi_1) = \mathrm{sgn}(\chi_2)$, the related wavelength is occasionally smaller than or comparable to the periodicity of the metamaterials and hence may be greatly degraded by the scattering from imperfections. Thus, long-distance propagation of HSSs in the second case may not be stable under practical considerations.

4. Measurement

For MM1 and MM2, there exist four combinations for exciting the HSS, that is, MM1+MM1(ZR), MM2+MM2(ZR), MM1+MM2(ZR), and MM1+MM2. Here, the abbreviation MM1+MM1(ZR) or MM2+MM2(ZR) represents the combination of MM bulks that only MM1 or MM2 is applied with half of the metamaterial being z-reversed; MM1+MM2(ZR) represents the combination that MM1 and MM2 bulks are placed together, with MM2 being z-reversed, so $\mathrm{sgn}(\chi_1) = -\mathrm{sgn}(\chi_2)$; MM1+MM2 represents the combination that MM1 and MM2 bulks are placed together, with $\mathrm{sgn}(\chi_1) = \mathrm{sgn}(\chi_2)$. The photos of MM1 and MM2 as well as the MM1+MM2 composites are shown in **Figure 4**a. In the experimental setup, two layers of the metamaterial bricks are stacked in the z-direction, which is sufficient to observe the HSS because most of the EM power is confined to the space in between two adjacent layers according to our simulations.

In the measurements, we put different metamaterials together and measured the transmittance between two z-polarized dipoles using the Vector Network Analyzer (VNA). First, the transmittance from MM1 and MM2 is tested to determine the forbidden bands of the metamaterials. The measured curves are presented as the two dashed lines in Figures 4b,c. We see that suppressed transmission with overlapping occurs in the range from 2.45 to 2.65 GHz, a frequency band that roughly satisfies the designed forbidden (bright) region. Next, the transmission from the MM1+MM1(ZR) and MM2+MM2(ZR) composites is measured, and shown as solid lines in Figure 4b. It is obvious that the HSSs are successfully excited and that the power transmittance is significantly increased across the entire forbidden band. Finally, the transmission from the MM1+MM2(ZR) and MM1+MM2 composites is measured and presented as the solid lines in Figure 4c. Whereas we expect that the HSS will be excited across the entire forbidden band for the MM1+MM2(ZR) case, it is excited at only a part of the forbidden band for the MM1+MM2 case. We also observe that the HSS in the MM1+MM2 composite suffers from strong attenuation if we lengthen the propagation passage. This is because the HSS wavelength is comparable to the periodicity of the two metamaterials, and thus, its propagation is greatly influenced by the scattering from imperfections as well as the

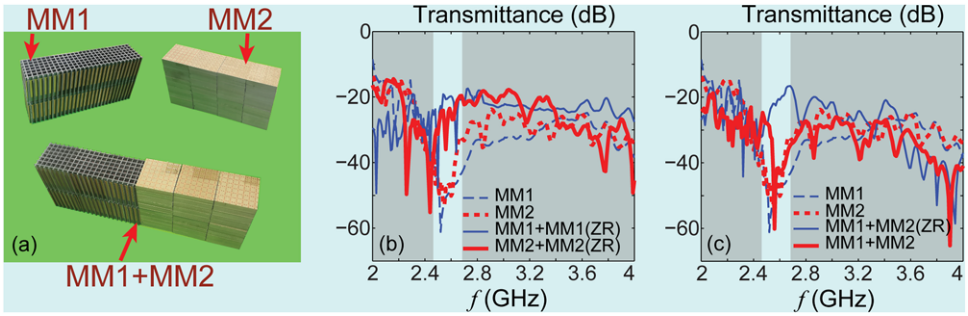

Figure 4. a) MM1, MM2 and MM1+MM2 bulks in the experiments. b) Measured transmittance for MM1, MM2, MM1+MM1(ZR), and MM2+MM2(ZR) composites. The forbidden band is observed from 2.45 GHz to 2.65 GHz. The HSSs are successfully excited across the entire forbidden. c) Measured transmittance for MM1, MM2, MM1+MM2(ZR), and MM1+MM2 composites. From the transmittance, the HSS is excited across the entire forbidden band for the MM1+MM2(ZR) composite but only part of the forbidden band (at approximately 2.5 GHz) for the MM1+MM2 composite. We observe in the experiments that the HSS in the MM1+MM2 composite is very sensitive to the combining details and losses and vanish much faster than in the other cases.

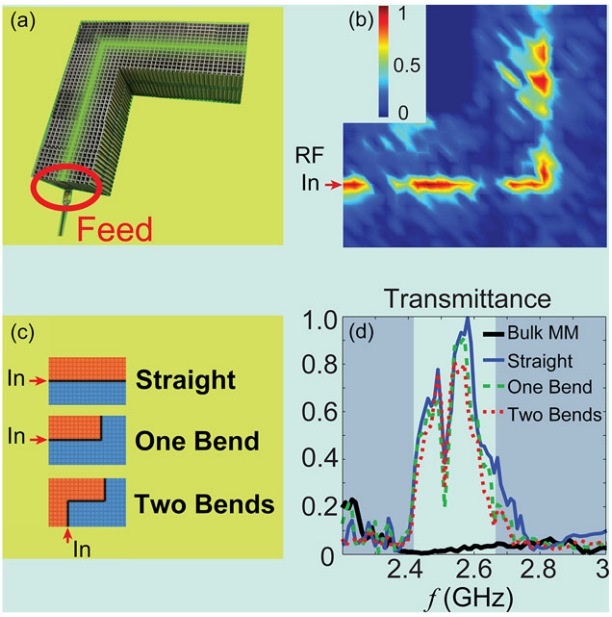

Figure 5. The experiments on backscattering suppression by the HSS. a) An image of the building block of the HSS passage. The passage of the HSS is indicated in green. b) Real part of the measured E_z at 2.55 GHz for an HSS encountering a 90° corner. c) The schematics of three HSS passages in the experiments: straight case, one-bend case, and two-bend case. d) The measured transmittance (normalized and with a linear scale). Inside the forbidden band (2.45–2.65 GHz), the three curves almost overlap, indicating the low level reflection by the corners. In the figure, all the transmittances are normalized by the maximum value of the straight case.

inevitable losses. Additional simulations demonstrating this effect can be found in Supporting Information.

Next, we test the backscattering suppression of the HSS. Here, the MM1+MM1(ZR) composite is used in the measurement. This is because only MM1 has sufficiently large intervals for allowing the insertion of detecting probes (vertically aligned) so that the electric field can be recorded. In the measurements, the feeding probe is placed horizontally at one terminal of the sample, as shown in the lower part of **Figure 5**a. Since the HSS is pseudo-spin-like and hardly matched to the free space, the external reflection at the two passage terminals is inevitable. To overcome this, the feeding probe is embedded into the metamaterial sample so that the phase interference for the propagating waves is broken. In Figure 5b, the real part of the measured E_z in the HSS with a 90° corner is presented. We see that the HSS is well confined along the interface, and the influence of the 90° corner is weak, considering the imperfect fabrication and the strong localized fields.

The low-level reflection may be quantitatively determined through the power transmission experiments. Here, we design three HSS passages, that is, the straight case, the one-bend case, and the two-bend case, as depicted in Figure 5c. To make the measurements comparable, the overall length of each passage is identical. In Figure 5d, the normalized transmittances for the three passages are shown. For comparison, the transmittance by a homogeneous metamaterial sample is also recorded. We see that without the HSS passage, the transmission is rather low. With the HSS passages, the transmission is increased. The large contrast in transmission indicates the successful excitation of the HSS in the forbidden region. In the three HSS cases, the transmittance varies in the forbidden band, which is mainly determined by the frequency-selective profile of the whole transmitting and receiving system. The consistency of the transmission for the three cases is observed in the wide frequency band, indicating the low-level (nearly zero) reflection from the corner(s).

5. Discussions

We note that in our platform, the pseudo-spin states (made by hybridizing all the polarizations) on the boundary cannot behave gauge invariant in the interior of the metamaterials, due to the fact that the metamaterials' $\bar{\bar{\varepsilon}}$ and $\bar{\bar{\mu}}$ are not necessarily identical or matched, thus the TE-like and TM-like modes may not share the same dispersion diagram. Hence, a topological invariant to the bulk metamaterials may not be valid, even though the numerical calculation may still be possible based on the approaches reported in Refs. 34,35. At a single frequency, the metamaterials studied may not create a spatial dispersion gap in-between the TE-like and the TM-like modes,[22] because of their close-curved dispersions in the x-y plane. Moreover, with MM1, MM2 can be

conveniently obtained by gradually changing both the substrate's dielectric constant and the dimensions of the metallic structures, and vice versa. For the entire process, the MM's forbidden band is never closed and is used in the experiments (i.e., the MM1+MM2 case). For all the above reasons, we realize that no topological transition is involved in the whole system.

Also note that our description is classical and only relies on the bulk's effective parameters; we could also image that certain disordered metamaterials could work as well. The flexibility of the proposed scheme allows extensions to any other frequency bands such as terahertz and optical ranges. For instance, nanostructured metamaterials with similar bianisotropy are easily produced through planar lithography and operate in the terahertz and optical ranges.[36–39]

6. Conclusion

In conclusion, we reveal the excitation of spin momentum–locked HSS by homogeneous bianisotropic metamaterials, that is, an interface formed by two metamaterial bulks with large bianisotropy contrast ensuring the HSS. According to the theoretical formulation and numerical simulations, the specified HSS behave as pseudo-spin states and are capable of dramatically suppressing backscattering, provided the pseudo-spin is preserved during propagation. With the enhanced bianisotropy, the metamaterials would be totally forbidden so that the HSS are well confined. Since no exact global symmetry protection is found during the process, the implementation of spin momentum–locked HSS is found to be convenient. Our work exhibits an example to emulate spin momentum–locked pseudo-spin states by conventional forbidden materials without topological transition, which would be greatly beneficial for future photonic controls.

Supporting Information

Supporting Information is available from the Wiley Online Library or from the author.

Acknowledgements

The authors are grateful for the fruitful discussion with Dr. W. J. Chen at Hong Kong University of Science and Technology and Prof. L. Lu at the Chinese Academy of Sciences. This work was financially supported by the National Natural Science Foundation of China (NSFC, Grant No. 61372022, Grant No. 61401395, and Grant No. 61405067) and the Natural Science Foundation of Zhejiang Province (ZJNSF, Grant No. LY13F010020). Work at Ames Laboratory was partially supported by the U.S. Department of Energy, Office of Basic Energy Science, Division of Materials Sciences and Engineering under Contract No. DE-AC02-07CH11358, the U.S. Office of Naval Research Award No. N00014-14-1-0474 (simulations), and the European Research Council under the ERC Advanced Grant No. 320081 (PHOTOMETA) supported work (theory) at FORTH.

Conflict of Interest

The authors declare no conflict of interest.

Keywords

bianisotropy, electromagnetic metamaterials, photonic surface states, pseudo-spins, scattering-less transmission

Received: January 2, 2018
Revised: May 16, 2018
Published online: June 19, 2018

[1] C. L. Kane, E. J. Mele, *Phys. Rev. Lett.* **2005**, *95*, 146802.
[2] M. Z. Hasan, C. L. Kane, *Rev. Mod. Phys.* **2010**, *82*, 3045.
[3] X. L. Qi, S. C. Zhang, *Rev. Mod. Phys.* **2011**, *83*, 1057.
[4] B. A. Bernevig, T. L. Hughes, *Topological Insulators and Topological Superconductors*, Princeton University Press, Princeton and Oxford **2013**.
[5] L. Lu, J. D. Joannopoulos, M. Soljačić, *Nat. Photon.* **2014**, *8*, 821.
[6] F. Haldane, S. Raghu, *Phys. Rev. Lett.* **2008**, *100*, 013904.
[7] Z. Wang, Y. Chong, J. Joannopoulos, M. Soljačić, *Phys. Rev. Lett.* **2008**, *100*, 013905.
[8] K. X. Liu, L. F. Shen, S. He, *Opt. Lett.* **2012**, *37*, 4110.
[9] A. B. Khanikaev, S. H. Mousavi, W.-K. Tse, M. Kargarian, A. H. MacDonald, G. Shvets, *Nat. Mater.* **2012**, *12*, 233.
[10] W. J. Chen, S. J. Jiang, X. D. Chen, B. Zhu, L. Zhou, J. W. Dong, C. T. Chan, *Nat. Commun.* **2014**, *5*, 5782.
[11] K. Y. Bliokh, F. Nori, *Phys. Rep.* **2015**, *592*, 1.
[12] K. Y. Bliokh, F. J. Rodríguez-Fortuño, F. Nori, A. V. Zayats, *Nat. Photon.* **2015**, *9*, 796.
[13] K. Y. Bliokh, A. Y. Bekshaev, F. Nori, *Nat. Commun.* **2014**, *5*, 3300.
[14] K. Y. Bliokh, F. J. Rodríguez-Fortuño, A. Y. Bekshaev, Y. S. Kivshar, F. Nori, *Opt. Lett.* **2018**, *43*, 963.
[15] T. A. Morgado, M. G. Silveirinha, arXiv:1711.08367, **2017**.
[16] C. Triolo, A. Cacciola, S. Patanè, R. Saija, S. Savasta, F. Nori, *ACS Photon.* **2017**, *4*, 2242.
[17] K. Y. Bliokh, D. Smirnova, F. Nori, *Science* , **2015**, *348*, 1448.
[18] W. J. Chen, Z. Q. Zhang, J. W. Dong, C. T. Chan, *Nat. Commum.* **2015**, *6*, 8183.
[19] M. G. Silveirinha, *Phys. Rev. B* **2017**, *95*, 035153.
[20] A. V. Kats, S. Savel'ev, V. A. Yampol'skii, F. Nori, *Phys. Rev. Lett.* **2007**, *98*, 073901.
[21] A. Serdyukov, I. Semchenko, S. Tretyakov, A. Sihvola, *Electromagnetics of Bi-anisotropic Materials: Theory and Applications*, Gordon and Breach, Amsterdam, Netherlands **2001**.
[22] W. Gao, M. Lawrence, B. Yang, F. Liu, F. Fang, B. Béri, J. Li, S. Zhang, *Phys. Rev. Lett.* **2015**, *114*, 037402.
[23] R. Marqués, F. Medina, R. Rafii-El-Idrissi, *Phys. Rev. B 65*,144440 (**2002**).
[24] L. Jing, Z. Wang, R. Maturi, B. Zheng, H. Wang, Y. Yang, L. Shen, R. Hao, W. Yin, E. Li, H. Chen, *Laser Photonics Rev*. **2017**, *11*, 1700115.
[25] Q. H. Guo, W. L. Gao, J. Chen, Y. M. Liu, S. Zhang, *Phys. Rev. Lett.* **2015**, *115*, 067402.
[26] J. A. Kong, *Electromagnetic Wave Theory*, EMW Publishing, Cambridge, MA: **2005**.
[27] J. D. Jackson, *Classical Electrodynamics*, John Wiley & Sons, Hoboken, NJ **1999**.
[28] J. A. Kong, *Proc. IEEE* **1972**, *60*, 1036.
[29] J. B. Pendry, A. J. Holden, D. J. Robbins, W. J. Stewart, *IEEE Micro. Theory Technol.* **1999**, *47*, 2075.
[30] R. A. Shelby, D. R. Smith, S. Schultz, *Science* **2001**, *292*, 77.
[31] C. É. Kriegler, M. S. Rill, S. Linden, M. Wegener, *IEEE J. Sel. Top. Quantum Electron.* **2010**, *16*, 2.
[32] A. Alù, *Phys. Rev. B* **2011**, *84*, 075153.
[33] J. W. Dong, M. L. Chang, X.-Q. Huang, Z. H. Hang, Z. C. Zhong, W. J. Chen, Z. Y. Huang, C. T. Chan, *Phys. Rev. Lett.* **2015**, *114*, 163901.

[34] M. G. Silveirinha, *Phys. Rev. B* **2015**, *92*, 125153.
[35] M. G. Silveirinha, *Phys. Rev. B* **2016**, *93*, 075110.
[36] C. E. Kriegler, M. S. Rill, M. Thiel, E. Müller, S. Essig, A. Frölich, G. Freymann, S. Linden, D. Gerthsen, H. Hahn, K. Busch, M. Wegener, *Appl. Phys. B*, **2009**, *96*, 749.
[37] M. S. Rill, C. E. Kriegler, M. Thiel, G. Freymann, S. Linden, M. Wegener, *Opt. Lett.* **2009**, *34*, 19.
[38] Z. Liu, Z. Liu, J. Li, W. Li, J. Li, C. Gu, Z. Li, *Sci. Rep.* **2016**, *6*, 27817.
[39] K. Fan, A. C. Strikwerda, H. Tao, X. Zhang, R. D. Averitt, *Opt. Express* **2011**, *19*, 13, 12619.